Heliyon 9 (2023) e21303

Contents lists available at ScienceDirect

Heliyon

journal homepage: www.cell.com/heliyon

Research article

Non-polarized and ultra-narrow band filter in MIR based on multilayer metasurface

Wentian Chu [a,c], Xuepeng Xu [a,c], Chunfeng Cai [b,d,*], Huizhen Wu [e], Gang Bi [a,**]

[a] School of Information and Electrical Engineering, Hangzhou City University, No. 48, Huzhou Street, Hangzhou, 310015, China
[b] Fundation Science Education Center, Hangzhou City University, No. 48, Huzhou Street, Hangzhou, 310015, China
[c] College of Information Science and Electronic Engineering, Zhejiang University, No. 38, Zheda Road, Hangzhou, 310027, China
[d] State Key Lab of Silicon Materials, Zhejiang University, No. 38, Zheda Road, Hangzhou, 310027, China
[e] Department of Physics, Zhejiang University, No. 38, Zheda Road, Hangzhou, 310027, China

ARTICLE INFO

Keywords:
Artificial metamaterials
Mid infrared region
Ultra-narrow band filter

ABSTRACT

We propose an ultra narrow-band filter in the mid infrared region (MIR) using artificial metamaterials (AMM), which is suitable for the design of on-chip photonic spectrometers. 2-D rectangular holes with a cross-like layerout are adopted to enhance the filter's efficiency and precision. Considering the penetration depth of electromagnetic (EM) waves in the metal film, we opt for multi-layer films composed of metal layers and dielectric layers, instead of a single metal layer, to improve the structure's performance in the MIR. This multilayer configuration significantly enhances the efficiency and precision of the AMM structures in the MIR. The transmission peak, with a full width at half maximum (FWHM) of 30 nm, can be achieved and tuned in the wavelength range from 3.0 μm to 10.0 μm by changing the periods of the unit cell (enlarging the unit cell from 3.0 to 10.0 μm). The proposed AMM structures, with tunable narrow band transmittance in MIR, exhibit promising potential in the fabrication of narrow band photonic detectors and on-chip spectrometers.

1. Introduction

In contemporary applications, narrow-band detectors and on-chip spectrometers operating within the mid infrared region (MIR) have garnered significant interest due to their promising potential across a wide array of fields [1,2]. The mid-infrared region, spanning wavelengths from 3 to 30 μm, holds a distinctive status as the molecular fingerprint region. In this range, vital information about material structures is unveiled, offering indispensable insights for disciplines such as physical, chemical, and biological sciences [3–5]. Consequently, the demand for high-performance MIR detectors and spectrometers has escalated, not only within the realm of scientific research but also in everyday applications, military contexts, and even explorations beyond our planet. In these multifaceted applications, certain critical considerations emerge, primarily concerning the volume, weight, and cost of the devices to align them with their intended purposes. For applications in daily life, cost-efficiency is paramount, while in military deployments and space missions, the compactness and weight of the devices become pivotal factors. Traditional MIR spectrometers, relying on structures such as gratings or beam splitters within Michelson interferometers combined with optical dark cavities, have historically delivered

* Corresponding author at: Fundation Science Education Center, Hangzhou City University, No. 48, Huzhou Street, Hangzhou, 310015, China.
** Corresponding author at: School of Information and Electrical Engineering, Hangzhou City University, No. 48, Huzhou Street, Hangzhou, 310015, China.
E-mail addresses: caicf@hzcu.edu.cn (C. Cai), big@hzcu.edu.cn (G. Bi).

https://doi.org/10.1016/j.heliyon.2023.e21303
Received 9 July 2023; Received in revised form 19 October 2023; Accepted 19 October 2023

Available online 23 October 2023

high sensitivity and resolution. However, their inherent limitations, characterized by substantial volumes and high costs, render them unsuitable for contemporary demands. To overcome these challenges, the spotlight has shifted towards narrow-band detectors and on-chip spectrometers, marking these areas as vibrant areas of research [6]. Among these groundbreaking endeavors, ultranarrow band filters and microstructures exhibiting super absorption properties have emerged as focal points [7–9]. These innovations promise to revolutionize MIR detection and spectroscopy, offering streamlined, cost-effective, and portable solutions capable of meeting the diverse needs of scientific exploration, everyday applications, military operations, and space ventures.

Artificial metamaterials (AMM) have attracted significant attention due to their unique properties, including negative refractive indices [10], effective negative permeability [11], and perfect absorption effects spanning from the visible to THz regions [12–15]. They also exhibit properties of selective absorption [16] and extraordinary optical transmission effects (EOT) [17,18]. These effects arise from the resonance of optical modes, which typically feature narrow bands, enabling precise band selection in spectra. This resonance phenomenon is attributed to localized surface plasmons (LSP), which significantly enhance transmittance [19]. For instance, metamaterial-based perfect absorbers display exceptional absorption properties and tunable resonant wavelengths, making them invaluable in crafting narrow-band mid-infrared (MIR) detectors. Their nearly complete absorption renders them ideal for single-wavelength detectors [20,21] and thermal infrared (IR) detectors [22]. Fei Yi et al. [23] showcased multi-gas sensing using nanoantenna-integrated narrowband IR detectors without dispersive components, enhancing both their refinement and affordability. Additionally, Zao Yi et al. [14,24,25] demonstrated a multilayer nanodisc-structure solar absorber and thermal emitter with a bandwidth of 2929 nm and an average absorption efficiency of 97.4%. Their work, incorporating multilayer structures, significantly enhanced the absorption performance of nanodisc arrays. However, AMM structures exhibiting perfect absorption characteristics are unsuitable for photonic detectors because incident photons are absorbed and dissipated as heat. MIR photonic detectors like PbSe, HgCdTe, and InSb detectors rely on incident photons for efficient operation and thus require an alternative approach.

In this study, we introduce a nonpolarized and ultra-narrow band filter in the MIR based on a multi-layer AMM structure. Simulation results highlight the significant impact of AMM structure thickness on filter performance due to the extensive penetration depth of the electromagnetic field in the MIR. To enhance the quality of the AMM structures, we opt for multi-layers instead of a single layer, a crucial design choice that ensures high-quality performance. Additionally, our AMM structure demonstrates polarization-independent sensitivity and tunability across a broad wavelength range. Notably, Gao et al. [26] explored tunable extraordinary optical transmission in the terahertz regime using a nested structure of graphene and metallic ring-rods, while Du et al. [27] demonstrated exceptional optical transmission and sensing capabilities through metal nanohole and nanoparticle array coupling. Qin et al. [28] showcased the extraordinary optical transmission properties of bi-layered plasmonic nanostructure arrays. Our approach stands out by employing a multilayer architecture and rectangular holes, which introduce waveguide modes and shape resonances, leading to higher transmittance and a narrower full width at half maximum (FWHM) of the transmission peak. These findings hold promise for inspiring advancements in the development of single-wavelength detectors and on-chip spectrometers in the MIR.

2. Simulation models and methods

Klein Koerkamp's research delved into the impact of hole shape on extraordinary transmission through periodic arrays of subwavelength holes [29]. Both experiments and calculations demonstrated that transitioning from circular to rectangular holes significantly increased transmittance (EOT) by an order of magnitude in the visible range. This enhancement was attributed to the shape resonances of rectangular holes. In our study, we conducted a comparison of transmittance between circular, square, and rectangular holes in the MIR, as illustrated in Fig. 1(c). The circular and square holes had diameters and lengths set at 0.9 μm, while the rectangular hole's length (L) and width (W) were set at 1.1 μm and 0.9 μm, respectively. Surprisingly, despite the rectangular hole being only 1.2 times and 1.6 times larger in area than the square and circular holes, its transmittance surpassed theirs significantly. Specifically, the transmittance of the rectangular hole was 3.7 times and 13.3 times larger than that of the square and circular holes, respectively. To ensure nonpolarized characteristics of the AMM structures, we adopted a cross-like layout with symmetrically positioned rectangular holes in both the x and y directions. The schematic of the AMM structure is depicted in Fig. 1(a), where the hole's length (L) and width (W) are denoted. Fig. 1(b) reveals the partially enlarged details of the AMM structure, which is marked with a rectangular box in Fig. 1(a). The lattice period (P) is uniform in both x and y directions, with the distance (d) from the hole's center to the unit's center also indicated. Recognizing the significance of thickness in the z direction, we incorporated metal layers (M) and silica layers (S) to form the multi-layer MSMS..SM structure. Each layer had a thickness of 0.2 μm, contributing to the three-dimensional intricacy of the AMM design.

The optical properties of the AMM were computed using the three-dimensional (3D) finite-difference time-domain (FDTD) method. Fig. 1(d) displays the simulated transmission spectra of various metal materials employed as the metal layers in the three-layer AMM structures. Among these materials, silver (Ag) exhibited the most optimal performance. Consequently, in subsequent studies, we employed Ag as the default metal layer unless otherwise specified.

3. Results and discussion

Under normal incidence conditions, we calculated the transmission spectra and electric field intensity distributions. As depicted in Fig. 2(a), the blue, red, and black lines represent the transmission spectra of single, triple, and five-layer AMM structures, respectively. The AMM structure parameters were set at $L = 1.0$ μm, $W = 0.9$ μm, $d = 1.2$ μm, and $P = 4.0$ μm. For single and double-layer structures, the transmission spectra exhibited a Fano-like line shape [30]. The transmittance at the non-resonant band was high, and the FWHM

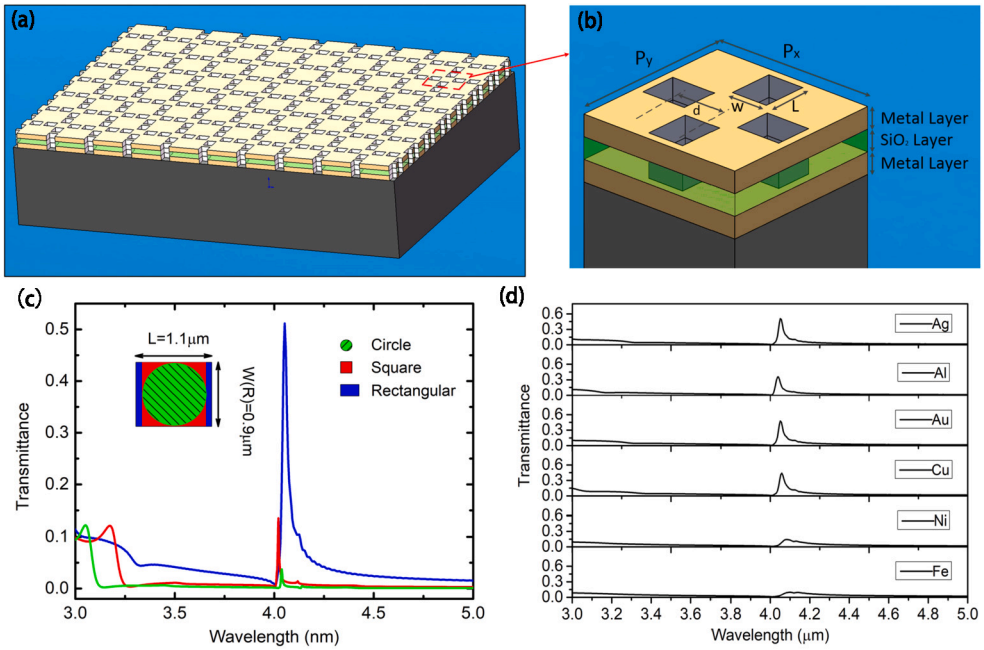

Fig. 1. (a) illustrates the three-dimensional schematic of the proposed AMM structure. (b) delineates the specific parameters of the AMM unit cell, where P_x and P_y denote the periods of the unit in the x and y directions, W and L represent the width and length of the hole, and d signifies the distance between the centers of the hole and the unit cell. (c) showcases the transmission spectra of arrays consisting of circles, squares, and rectangular holes. Lastly, (d) exhibits the simulated transmission spectra of different metal materials utilized as the metal layers.

of the transmission peak was large. Consequently, single and double-layer AMM structures were unsuitable for fabricating single-wavelength filters. In contrast, triple and four-layer AMM structures exhibited higher peak transmittance (50%) compared to single, double, and five-layer structures. This enhancement was attributed to the resonance of waveguide modes [31]. The FWHM of the triple-layer structure (30 nm at 4.0 μm) was smaller than that of the four-layer structure (58 nm at 4.2 μm). Notably, a redshift was observed in the two and four-layer structures. This redshift could be attributed to changes in localized surface plasmon (LSP) modes due to the absence of the metal layer cover, as depicted in Fig. 2(c, e) and (h, j). However, increasing the number of layers led to a rapid decrease in transmittance. In the case of the five-layer AMM structure, the peak transmittance decreased to 20%. Consequently, triple-layer structures exhibited the best performance. Fig. 2(b, g), (c, h), (d, i), (e, j) and (f, k) illustrate the electric field at the xy and xz directions at the resonant wavelength for each AMM structure, respectively. Strong electrical oscillations between the hole walls, attributed to LSP resonance, were observed in (b, c, d, e, f), causing extraordinary optical transmission effects [32]. Additionally, resonances from waveguide modes, leading to narrowed transmission peaks [33], were observed in Fig. 2(g, h, i, j, k). Taking the electric-magnetic field distributions of the triple-layer structure as an example, Fig. 2(d) illustrates the accumulation of opposite charges on the symmetrical edge, leading to a strong electric field in the y-direction on the inner wall of the rectangular hole. This accumulation results in electric dipole resonance. In Fig. 2(i), a strong coupling effect between the two silver layers induces electric dipole resonance, causing reverse currents to enter the two silver films, forming magnetic dipoles. These magnetic dipoles generate a robust magnetic resonance in the intermediate dielectric layer. The interaction between electric and magnetic dipoles reduces the energy loss of incident electromagnetic waves during transmission. Generally, the localized surface plasmon (LSP) generated by collective oscillations of conducting electrons is coupled to electric and magnetic dipoles. This coupling enhances the intensity of the local electromagnetic field and leads to the localization of the electromagnetic field, resulting in an extraordinary optical transmission (EOT) effect. Based on these calculated results, we adopt the triple-layer artificial metamaterial (AMM) structure in our subsequent work unless otherwise specified.

In Fig. 3, we calculated the transmission spectra of artificial metamaterial (AMM) structures with varying widths (a) or lengths (b) within the unit cell, while keeping the other parameters constant. In Fig. 3(a), the period of the AMM structures, the length of the hole, and d were set at 4.0 μm, 1.1 μm, and 1.15 μm, respectively. The width of the hole was varied from 0.7 to 1.1 μm. The positions of the transmission peaks exhibited a slight redshift. However, the transmittance in the short-wavelength band (3.0-3.5 μm) increased when the width of the hole was smaller or larger than 0.9 μm. In Fig. 3(b), we maintained the parameters as in Fig. 3(a), except for the length of the holes. The width of the holes was set at 0.9 μm, and the length of the holes was varied from 0.9 to 1.3 μm. Similar to the results shown in Fig. 3(a), a redshift in the transmission peaks was observed. These findings indicate that the resonance condition is not highly sensitive to the geometry of the holes, and the slight redshift of the transmission peak can be attributed to the change in waveguide resonance. Considering the performance of the mid-infrared (MIR) filter, it can be concluded that with a period of 4.0 μm and d of 1.1 μm, the length and width of the holes should be set at 1.1 μm and 0.9 μm, respectively.

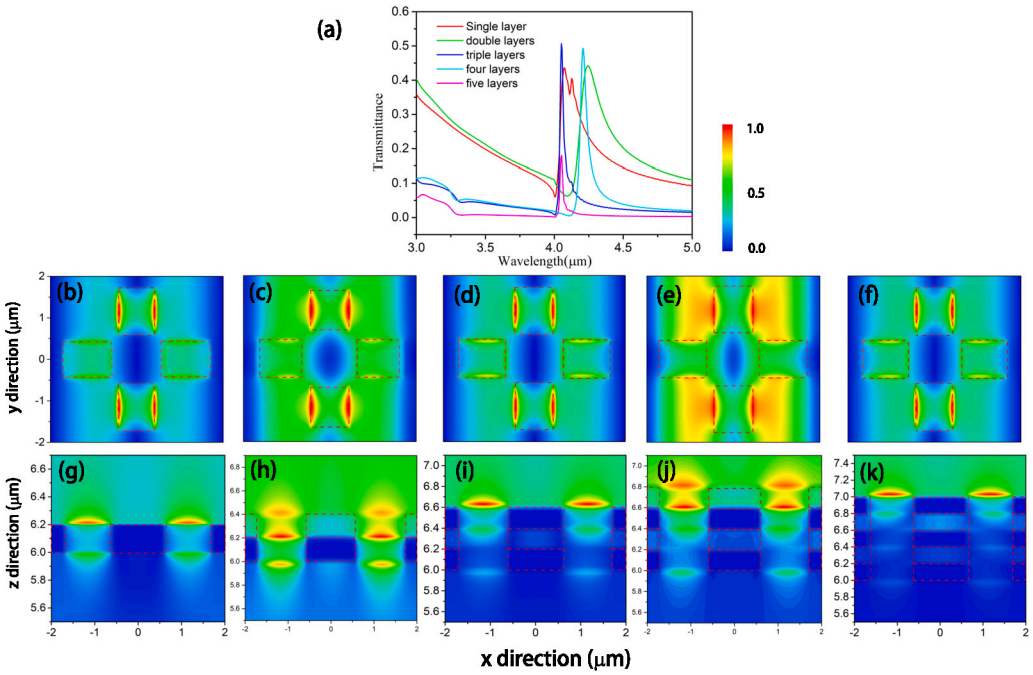

Fig. 2. (a) displays the calculated transmission spectra of artificial metamaterial (AMM) structures with different layers. Figures (b, c, d, e, f) depict the electric field distributions in the xy plane, while (g, h, i, j, k) illustrate the electric field distributions in the xz plane.

The tunability of the AMM structures can be achieved by varying the periods of the units. Two cases have been considered for discussion. Fig. 3(c) displays the normalized transmission spectra with the period varied from 3.7 to 4.3 μm, while the other parameters of the unit cell remain unchanged (W = 0.9 μm, L = 1.1 μm, and d = 1.15 μm). In this scenario, the position of the peak can be shifted from 3.77 to 4.33 μm. However, further increasing the period will lead to a rapid decline in the transmittance of the peak. Fig. 3(d) illustrates the normalized transmission spectra with the period varied from 3.0 to 10.0 μm, and the unit cell is varied proportionally. In this case, the transmission peak position can be tuned to cover the wavelength range of 3.0 to 10.0 μm with nearly the same FWHM. When light illuminates the surface of a metal layer, a surface current is generated, which is a transient effect. The distribution and oscillation frequency of the surface current are determined by the boundary conditions of the electromagnetic field on the metal surface. Under the condition of a 2-D periodic aperture array structure, the induced surface plasmon waves (SPW) can be re-scattered by metal hole arrays and form transmitted photons through holes, resulting in the extraordinary optical transmission (EOT) effect. The dispersion of the SPW can be expressed as Eq. (1):

$$k_{sp} = k_0 \sqrt{\frac{\epsilon_1 * \epsilon_2}{\epsilon_1 + \epsilon_2}} \tag{1}$$

where k_{sp} and k_0 are the SPW and incident light, respectively. ϵ_i is the dielectric constant for the metal layer (i = 1) and dielectric layer (i = 2). The 2-D periodic aperture array will scatter the SPW and modify the propagation wave vector, as shown in eq. (2).

$$k_{sp_x} = k_x + iG_x + jG_y \tag{2}$$

where k_x is the propagating wave vector of light, i (j) is an integer. $G_x = 2pi/P_x$ and G_y are the reciprocal lattice vector of the hole array in x and y direction, respectively. According to Eq. (1) and Eq. (2), the wavelength of the steady-state surface plasmon waves (SPW) is dependent on the period of the scattering structure. Reference [29] suggests that the extraordinary light transmission of periodic hole arrays is strongly influenced by the hole shape, attributed to the shape resonance. Subwavelength deep holes can also produce waveguide effects. According to waveguide theory, the dispersion of the waveguide mode in a rectangular hole can be expressed as Eq. (3):

$$k_z^2 = \frac{2\pi}{\lambda}^2 - \frac{m^2\pi^2}{a^2} - \frac{n^2\pi^2}{b^2} \tag{3}$$

where k_z is the longitudinal wave vector, m and n are integer, and a and b are the length of the rectangle. For a certain thickness of the metal film, the longitudinal wave vector k_z is relatively constant. Increasing the size of the waveguide cross-section (i.e., the side length W or L of the small hole) will cause the wavelength λ to increase accordingly. As illustrated in Fig. 3(a, b), when W or L is increased, the transmission peaks exhibit a significant redshift.

Fig. 4(a) illustrates the angle resolution spectra of the AMM structure. The AMM structure exhibits significant dispersion properties due to its nature as 2D optical lattices. With an increasing incident angle, the transmission peak splits into two peaks, revealing a

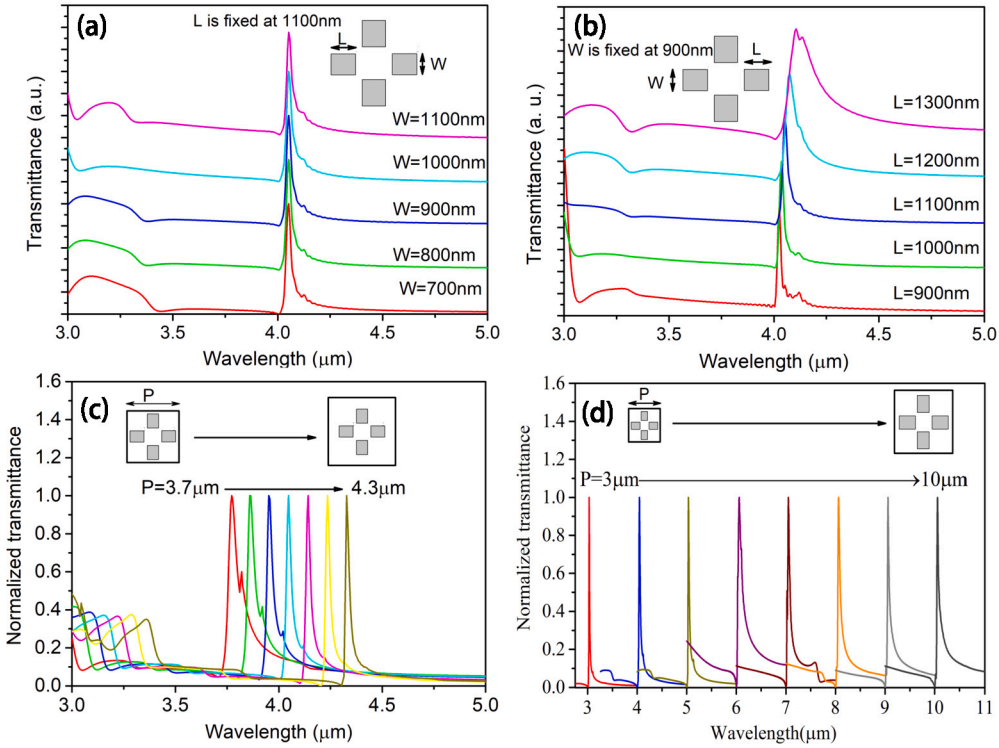

Fig. 3. (a, b) display the normalized transmission spectra of AMM structures concerning the widths/lengths of the holes, without changing the size of the unit, while maintaining the length/width fixed at 1.1 μm/0.9 μm, and setting the period of the unit cell and d at 4.0 μm and 1.15 μm, respectively. For clarity, the spectral lines are vertically shifted. (c, d) illustrate the normalized transmission spectra versus the periods of the unit cell, with the other parameters unchanged (c) and the other parameters changed proportionally (d).

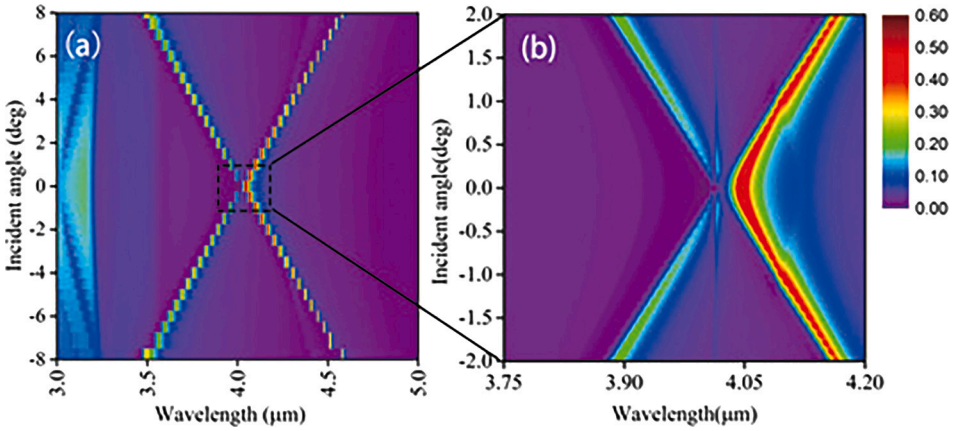

Fig. 4. (a) displays the angle resolution spectra of the artificial metamaterial (AMM) structure. (b) reveals the partially enlarged details of the cross structure in the angle resolution spectra, which is marked with a rectangular box in (a).

cross-like structure in the dispersion relation. In Fig. 4(b), we zoom in on the details of the cross structure and observe both leaky and nonleaky edges [34]. Magnusson et al. [35] have discussed the band flip and closure effects of the leaky and nonleaky modes by adjusting the parameters of optical lattices, both in numerical calculations and experiments. Our results are consistent with their findings, indicating that leaky and nonleaky modes exist in 2D rectangular hole arrays with a cross-like layout and are sensitive to the symmetry of the structures.

Fig. 5 depicts the calculated response spectra of the PbSe detector combined with AMM structures of various periods. The inset illustrates the schematic of the device. A buffer layer is initially deposited atop the PbSe detector to safeguard the device. Subsequently, the AMM structure is fabricated on top of the buffer layer. Through the incorporation of AMM structures, PbSe detectors exhibit excellent performance as single wavelength detectors, with tunable detecting wavelengths ranging from 2.0 to 6.0 μm.

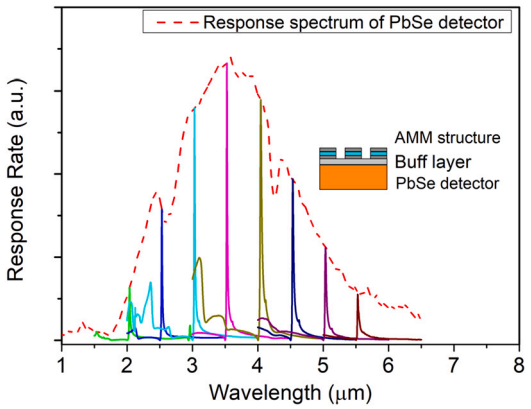

Fig. 5. Figure displays the calculated response spectra of the PbSe detector combined with AMM structures of varying periods. The inset illustrates the schematic of the device.

4. Conclusion

In summary, we propose an ultra-narrow band filter in MIR suitable for designing single wavelength detectors and on-chip photonic spectrometers. This work demonstrates 2-D rectangular hole arrays in the xy plane with a cross-like layout. The cross-like layout renders the structure polarization-insensitive to incident photons, and the multilayer structures significantly enhance filter performance due to electromagnetic waveguide resonance. The structure achieves a transmission peak with a transmittance of 50% and a FWHM of 30 nm. The position of the transmission peak can be tuned from 3.0 to 10.0 μm by varying the unit cell period from 3.0 to 10.0 μm. The angle resolution spectra of the structure exhibit dispersion features and the leaky mode of 2D structures. The calculated response spectra of the PbSe detector combined with the AMM structure indicate that the AMM structure demonstrated in this work is suitable for developing single wavelength detectors and on-chip photonic spectrometers in the MIR.

CRediT authorship contribution statement

Wentian Chu: Writing – original draft, Software, Data curation. **Xuepeng Xu:** Software, Investigation. **Chunfeng Cai:** Writing – review & editing, Supervision, Methodology, Formal analysis, Conceptualization. **Huizhen Wu:** Data curation. **Gang Bi:** Writing – review & editing, Supervision.

Declaration of competing interest

The authors declare that they have no known competing financial interests or personal relationships that could have appeared to influence the work reported in this paper.

Data availability

Data will be made available on request.

Acknowledgements

This work was supported by the Basic Research Supporting Project of Zhejiang University City College (No. J-202208).

References

[1] A. Kamboj, L. Nordin, A.J. Muhowski, D. Woolf, D. Wasserman, Room-temperature mid-wave infrared guided-mode resonance detectors, IEEE Photonics Technol. Lett. 34 (11) (2022) 615–618, https://doi.org/10.1109/LPT.2022.3175110.
[2] T.L. Roellig, C.W. McMurtry, T.P. Greene, T. Matsuo, I. Sakon, J.G. Staguhn, Mid-infrared detector development for the Origins Space Telescope, J. Astron. Telesc. Instrum. Syst. 6 (4) (2020) 041503, https://doi.org/10.1117/1.JATIS.6.4.041503.
[3] J.M. Charsley, M. Rutkauskas, Y. Altmann, V. Risdonne, M. Botticelli, M.J. Smith, C.R.T. Young, D.T. Reid, Compressive hyperspectral imaging in the molecular fingerprint band, Opt. Express 30 (10) (2022) 17340–17350, https://doi.org/10.1364/OE.451380.
[4] J. Zhu, S. Jiang, Y. Xie, F. Li, L. Du, K. Meng, L. Zhu, J. Zhou, Enhancing terahertz molecular fingerprint detection by a dielectric metagrating, Opt. Lett. 45 (8) (2020) 2335–2338, https://doi.org/10.1364/OL.389045.
[5] L. Maidment, P.G. Schunemann, D.T. Reid, Molecular fingerprint-region spectroscopy from 5 to 12 μm using an orientation-patterned gallium phosphide optical parametric oscillator, Opt. Lett. 41 (18) (2016) 4261–4264, https://doi.org/10.1364/OL.41.004261.
[6] T. Dong, Y. Yin, X. Nie, P. Jin, T. Li, H. Zhen, W. Lu, Narrow-band and peak responsivity enhanced metal microcavity quantum well infrared detector, Appl. Phys. Lett. 121 (2022) 073507, https://doi.org/10.1063/5.0099568.
[7] K.-C. Lin, M.-R. Tang, C.-F. Lin, S.-C. Lee, C.-T. Lin, Surface-plasmon-resonance based narrow-bandwidth infrared carbon monoxide detection system, IEEE Sens. J. 22 (10) (2022) 9803–9810, https://doi.org/10.1109/JSEN.2022.3164446.

[8] J. Zhang, K. Pan, J. Qiu, Mie-resonance-based metamaterials with perfect absorption in the terahertz frequency range, Phys. Status Solidi RRL 15 (4) (2021) 2100031, https://doi.org/10.1002/pssr.202100031.
[9] Z. Ren, R. Liu, Y. Zhang, T. Liu, F. Li, X. Hong, Y. Guo, Nonpolarizing narrow band metamaterial transmission filter based on electromagnetically induced transparency at visible wavelengths, Mater. Lett. 296 (2021) 129832, https://doi.org/10.1016/j.matlet.2021.129832.
[10] M. Liu, E. Plum, H. Li, S. Li, Q. Xu, X. Zhang, C. Zhang, C. Zou, B. Jin, J. Han, W. Zhang, Temperature-controlled optical activity and negative refractive index, Adv. Funct. Mater. 31 (14) (2021) 2010249, https://doi.org/10.1002/adfm.202010249.
[11] X. Cai, G. Hu, Grating effect in negative permeability meta-material, Phys. Lett. A 372 (15) (2008) 2692–2695, https://doi.org/10.1016/j.physleta.2007.12.016.
[12] P. Grimm, G. Razinskas, J.-S. Huang, B. Hecht, Driving plasmonic nanoantennas at perfect impedance matching using generalized coherent perfect absorption, Nanophotonics 10 (7) (2021) 1879–1887, https://doi.org/10.1515/nanoph-2021-0048.
[13] D. Zhang, P. Zhu, X. Xie, Y. Liang, Q. Yang, M. Sun, X. Liang, J. Kang, H. Zhu, A. Guo, Q. Gao, Y. Yi, L. Li, C. Liu, J. Zhu, Tunable plasma narrow-band filter for ultrafast high-power lasers, Appl. Phys. Express 14 (12) (2021) 122001, https://doi.org/10.35848/1882-0786/ac33c5.
[14] Y. Zheng, Z. Yi, L. Liu, X. Wu, H. Liu, G. Li, L. Zeng, H. Li, P. Wu, Numerical simulation of efficient solar absorbers and thermal emitters based on multilayer nanodisk arrays, Appl. Therm. Eng. 230 (2023) 120841, https://doi.org/10.1016/j.applthermaleng.2023.120841.
[15] Z. Chen, P. Cai, Q. Wen, H. Chen, Y. Tang, Z. Yi, K. Wei, G. Li, B. Tang, Y. Yi, Graphene multi-frequency broadband and ultra-broadband terahertz absorber based on surface plasmon resonance, Electronics 12 (12) (2023), https://doi.org/10.3390/electronics12122655.
[16] J. Wu, Enhancement of THz absorption in monolayer graphene for light at Brewster angle incidence, Phys. Lett. A 383 (35) (2019) 125994, https://doi.org/10.1016/j.physleta.2019.125994.
[17] C. Tardieu, T. Estruch, G. Vincent, J. Jaeck, N. Bardou, S. Collin, R. Haidar, Extraordinary optical extinctions through dual metallic gratings, Opt. Lett. 40 (4) (2015) 661–664, https://doi.org/10.1364/OL.40.000661.
[18] W. Jia, X. Liu, Mechanism of the superenhanced light transmission through 2d subwavelength coaxial hole arrays, Phys. Lett. A 344 (6) (2005) 451–456, https://doi.org/10.1016/j.physleta.2005.06.094.
[19] M. Sun, R.-J. Liu, Z.-Y. Li, B.-Y. Cheng, D.-Z. Zhang, H. Yang, A. Jin, Enhanced near-infrared transmission through periodic h-shaped arrays, Phys. Lett. A 365 (5) (2007) 510–513, https://doi.org/10.1016/j.physleta.2007.01.033.
[20] Q. Li, J. Lu, P. Gupta, M. Qiu, Engineering optical absorption in graphene and other 2d materials: advances and applications, Adv. Opt. Mater. 7 (20) (2019) 1900595, https://doi.org/10.1002/adom.201900595.
[21] S.G. Zamharir, R. Karimzadeh, X. Luo, Tunable polarization-independent MoS_2-based coherent perfect absorber within visible region, J. Phys. D, Appl. Phys. 54 (16) (2021) 165104, https://doi.org/10.1088/1361-6463/abdd68.
[22] S. Ogawa, M. Kimata, Wavelength- or polarization-selective thermal infrared detectors for multi-color or polarimetric imaging using plasmonics and metamaterials, Materials 10 (5) (2017), https://doi.org/10.3390/ma10050493.
[23] T. Xiaochao, Z. Heng, L. Junyu, W. Haowei, G. Qiushi, Z. Houbin, L. Huan, Y. Fei, Non-dispersive infrared multi-gas sensing via nanoantenna integrated narrowband detectors, Nat. Commun. 11 (2020) 5245, https://doi.org/10.1038/s41467-020-19085-1.
[24] F. Wu, P. Shi, Z. Yi, H. Li, Y. Yi, Ultra-broadband solar absorber and high-efficiency thermal emitter from UV to mid-infrared spectrum, Micromachines 14 (5) (2023), https://doi.org/10.3390/mi14050985.
[25] Y. Zhu, P. Cai, W. Zhang, T. Meng, Y. Tang, Z. Yi, K. Wei, G. Li, B. Tang, Y. Yi, Ultra-wideband high-efficiency solar absorber and thermal emitter based on semiconductor InAs microstructures, Micromachines 14 (8) (2023).
[26] Z. Gao, Y. Shi, M. Li, J. Song, X. Liu, X. Wang, F. Yang, Tunable extraordinary optical transmission with graphene in terahertz, ACS Omega 6 (44) (2021) 29746–29751.
[27] B. Du, Y. Yang, Y. Zhang, P. Jia, H. Ebendorff-Heidepriem, Y. Ruan, D. Yang, Enhancement of extraordinary optical transmission and sensing performance through coupling between metal nanohole and nanoparticle arrays, J. Phys. D, Appl. Phys. 52 (27) (2019) 275201, https://doi.org/10.1088/1361-6463/ab1835.
[28] Y. Qin, J. He, F. Yang, Z. Zhang, Z. Yuan, M. Wu, Extraordinary optical transmission properties of a novel bi-layered plasmonic nanostructure array, Optik 174 (2018) 684–691, https://doi.org/10.1016/j.ijleo.2018.08.073.
[29] K.K. Koerkamp, S. Enoch, F.B. Segerink, N. Van Hulst, L. Kuipers, Strong influence of hole shape on extraordinary transmission through periodic arrays of subwavelength holes, Phys. Rev. Lett. 92 (18) (2004) 183901, https://doi.org/10.1103/PhysRevLett.92.183901.
[30] C. Cai, G. Bi, T. Xu, Fano resonance in the CsPbBr nanocrystal/Ag nanostructure through the exciton-plasmon coupling, Appl. Phys. Lett. 115 (16) (Oct. 2019), https://doi.org/10.1063/1.5124408.
[31] P. Gu, J. Chen, C. Yang, Z. Yan, C. Tang, P. Cai, F. Gao, B. Yan, Z. Liu, Z. Huang, Narrowband light reflection resonances from waveguide modes for high-quality sensors, Nanomaterials 10 (10) (2020), https://doi.org/10.3390/nano10101966.
[32] S. Kasani, K. Curtin, N. Wu, A review of 2d and 3d plasmonic nanostructure array patterns: fabrication, light management and sensing applications, Nanophotonics 8 (12) (2019) 2065–2089, https://doi.org/10.1515/nanoph-2019-0158.
[33] A.S. Saleh, N. Raveu, Transmission peak at low frequencies by a fractal distribution of metamaterials layers in free space, Microw. Opt. Technol. Lett. 49 (1) (2007) 105–109, https://doi.org/10.1002/mop.22048.
[34] Y. Ding, R. Magnusson, Band gaps and leaky-wave effects in resonant photonic-crystal waveguides, Opt. Express 15 (2) (2007) 680–694, https://doi.org/10.1364/OE.15.000680.
[35] N. Razmjooei, R. Magnusson, Experimental band flip and band closure in guided-mode resonant optical lattices, Opt. Lett. 47 (13) (2022) 3363–3366, https://doi.org/10.1364/OL.463350.